Understanding the role of monolayer graphene during long range shock strengthening of metal-graphene heterostructure

Sen Xiang [a,b], Xingtao Liu [a], Rong Xu [b], Kejie Zhao [b], Dong Lin [c], Fei Yin [d,**], Gary J. Cheng [a,e,*]

[a] *School of Industrial Engineering, Purdue University, West Lafayette, IN, 47906, USA*
[b] *School of Mechanical Engineering, Purdue University, West Lafayette, IN, 47906, USA*
[c] *Department of Industrial and Manufacturing Engineering, Kansas State University, Manhattan, KS, 66506, USA*
[d] *Hubei Key Laboratory of Advanced Technology for Automotive Components, Wuhan University of Technology, Wuhan, 430070, PR China*
[e] *School of Materials Engineering, Purdue University, West Lafayette, IN, 47906, USA*

ARTICLE INFO

ABSTRACT

Graphene has been extensively used in graphene reinforced metal composite, with strengthening effects due to its ability to block dislocation from propagation during the traditional low strain rate deformation process. Laser shock peening has been applied in graphene/metal composites with graphene concentration of 2–10% with a relatively close distance between the graphene layers. This work discovered a strong long-range coupling effects of graphene as a super-strong nanomaterial and shock-wave transmitter during laser shock processing under room temperature LSP and cryogenic temperature (cLSP), under extremely low graphene concentration (1.42×10^{-6}% vol.). Compared with simple compressed graphene-copper heterostructure, the yield strength of LSP and cLSP processed samples increases by 40%, and 76% respectively. We found that under laser shock peening (LSP) process, the shock wave can pass through long-distance to generate dislocation transportation from one layer to another graphene with the shock wave interaction between graphene layers separated very far away. Graphene plays an important role not only as a transmitter of shock waves, but also as a strong wall to bounce back shock waves to generate high dislocation density around graphene layers. We have designed experiments to compare the deformation behavior of the laminates under three deformation conditions: compression, LSP, and cLSP, respectively. It was found that the compressed sample has very few parallel dislocation arrays beneath the graphene interface, indicating that graphene blocks the dislocation movement and has very limited strengthening effects. The LSP processed samples contain much high dislocation density, while even higher density dislocation and strength are found in cLSP due to faster shock transportation in graphene/metal layers under cryogenic conditions. Finite element modeling was used to investigate the shock wave interaction with the graphene and metal layer under various conditions, which is consistent with experiments. Molecular dynamics simulation is used to simulate the microstructure of the laminates under various conditions and validated by experiments. This work provides a starting point to understand the long-range strengthening effects of 2D nanomaterials of extremely low concentrations and provide new design strategies for manufacturing graphene-metal nanocomposite and their strengthening approaches.

1. Introduction

The strengthening in metal matrix nanocomposite materials typically relies on the intrinsic strength and modulus of the reinforcing nanomaterials, in addition to other mechanisms such as dislocation hardening and grain boundary hardening. Graphene, as a single-atomic-layer material with extremely high intrinsic strength and modulus, has been extensively studied in graphene reinforced metal composite with strengthening mechanism due to its ability to block dislocation from propagation during traditional low strain rate deformation process. By direct current electrodeposition [1] or pulse electrodeposition [2], the graphene-copper composite film has been successfully developed. Laser

sintering is also utilized in the synthesis of single-layer graphene oxide and iron composite [3]. By dispersing 8 vol% graphene nanoplatelets in copper matrix with ball milling, yield strength is increased to 300 MPa compared to 150 MPa for pure copper [4].

Plastic deformation-induced dislocations and nanograins can further strengthen metal matrix nanocomposites. Recently, laser shock peening has been applied in additively manufactured graphene/metal composites with a graphene concentration of 2–10 wt% [5]. High-density dislocations and nanotwins are observed around graphene/iron interface and a 10% increase in Vickers hardness is achieved. During laser shock peening, a pulsed laser beam is focused on the top surface of the specimen, and plasma is formed. With plasma confined by glass media, the shock wave is generated and propagate into the specimen (shown in Fig. 1 a)). Since the shock wave will be attenuated as the depth increased, dislocation density is gradually reduced. Shock wave penetration depth is around 200um ~500um depending on the laser intensity and material properties [6]. The pulsed laser usually lasts for several nanoseconds and the corresponding shock wave lasts longer for several tens of nanoseconds. Due to the short pulse period, an extremely high strain rate ($\sim10^7 \ s^{-1}$) could be achieved.

To achieve better mechanical properties, metal matrix nanocomposite materials by mixing metal matrix and graphene require a larger amount of graphene. Mechanical behaviors of laminated graphene-metal structure have been studied in recent years with lower graphene concentration. Graphene-metal layered composites have been synthesized using graphene as the reinforcement due to its unique 2D layered structure. Kim [7] et al. successfully synthesized the graphene-copper nanolayered composites, and its high strength is ascribed to the dislocation pinning effect of graphene. Zhao [8] and Kumar [9] fabricated graphene-aluminum laminated composites using powder metallurgy technique and studied their mechanical properties and plastic deformation by micropillar compression tests. Hardness and strength can be improved in graphene-metal layered composites with a much smaller amount of graphene.

However, it will be difficult to further strengthen the metal below the graphene layer in graphene-metal laminated structures by conventional plastic deformation as dislocations cannot cross the graphene interface due to the ultra-strength of the graphene layer. Higher density dislocations are localized in the first metallic layer [7]. The dislocation evolution of graphene-metal layered composite after compression is presented in Fig. 1 b). In the beginning, a parallel array of dislocations is generated at the first metallic layer. As dislocations travel along the slip plane and approach the graphene interface, they will be blocked and piled up. Dislocation lines from other slip systems will form and interact with each other, generating new dislocations [10]. As compression continued, stress applied on the interface increase under the superposition of external stress and stress concentration introduced by the dislocation pile-up. When this stress is above the barrier stress to initiate dislocation emission, new dislocations can be generated at the neighboring layer (the second metallic layer). In this way, plastic deformation can transfer across the graphene interface. The barrier stress is quite large so that only low-density dislocations can be generated. As high-density dislocations are limited to the first metallic layer, strengthening effects of the material below the graphene layer by compression is limited.

Here, metal/graphene laminates with a graphene monolayer every 30-μm thickness of copper layer are processed by laser shock peening to study the long-range coupling effects of graphene as a super-strong nanomaterial and dislocation hardening during laser shock processing, under extremely low graphene concentration (1.42×10^{-6}% vol.). This process can be utilized to strengthen graphene-metal laminated structures since the plasma-induced shock wave can easily pass the graphene layer and plastically deform the metal layer beneath it. Fig. 1 c) shows the propagation of shock waves on laminated structures. When a shock wave interacts with the graphene layer, it is partially reflected instead of fully transmitted. Gradient dislocation nanostructures can be obtained eventually. Apart from strain rate, deformation temperature also has a pronounced effect on material properties [11,12]. By introducing low temperature during this process, cryogenic laser shock peening (cLSP) may further improve material strength by suppressing dynamic recovery.

It would be interesting to study the deformation mechanics, dislocation dynamics and microstructure, during shock wave propagation and its interaction with graphene during LSP of graphene copper laminates. Finite element method (FEM) had been extensively used for the prediction of residual stress distributions of metallic materials after LSP [13–15]. And shock wave propagation in pure copper had been illustrated by the in-depth stress evolution [16]. In Yang et al. 's recent work [17], shock response of titanium/carbon fibre laminates had been investigated with adhesive layers being inserted between titanium and carbon fibre and their mechanical behavior being defined based on the traction-separation law. Apart from shock wave propagation, dislocation evolutions were also of great importance. Molecular dynamics (MD) simulations had been widely used to study the dislocation behaviors
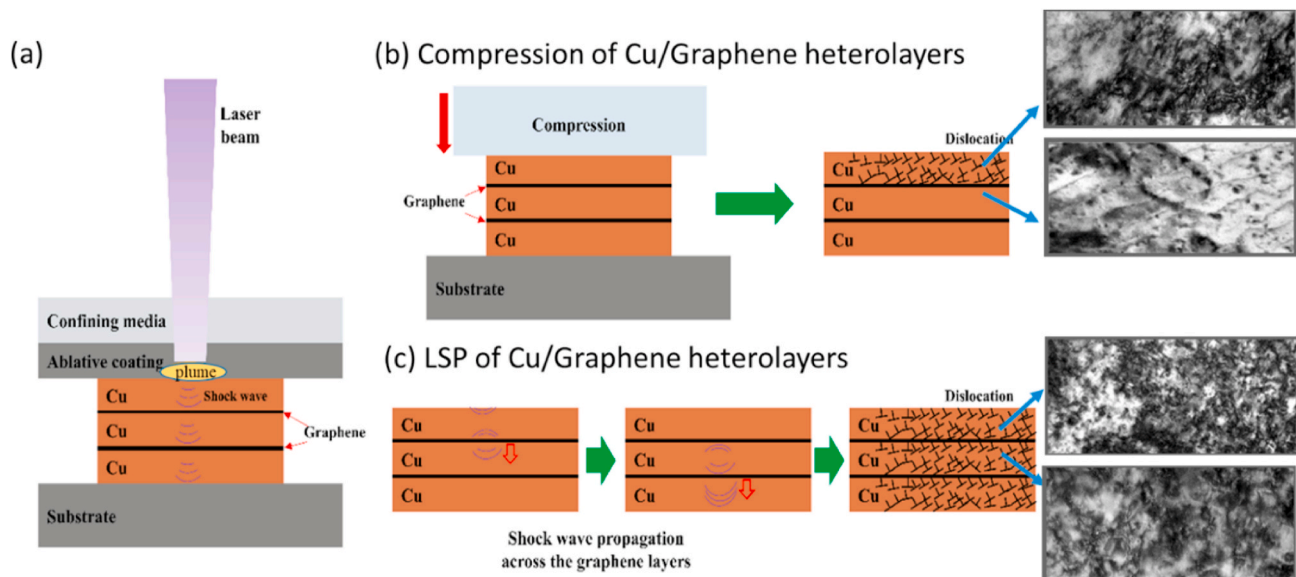

Fig. 1. a) Laser shock peening process. b) copper graphene composite under compression. c) copper graphene composite under laser shock peening.

[18]. Damadam et al. [19] and Salehinia et al. [20] investigated plastic deformation in Nb/NbC multilayers and found out that dislocations were firstly generated in the metal layers and then slip was transmitted from the Nb layer to the NbC layer. Graphene metal laminates under low strain rate load had also been studied using MD simulations: graphene-aluminum laminates under tensile stress [21], graphene-copper composites under compression [22], or cyclic shear loading [23]. Simulations had shown that dislocations were pinned by the graphene layer, thus could not propagate to the next layer during compression of copper and graphene composite [7]. For high strain rate process, Wang et al. investigated dislocation evolution and phase transition of single crystal iron under shock load with MD simulations [24], and Branicio et al. had found three shock response regimes for defect free single crystal AlN ceramics under different particle velocities [25].

In this work, we investigated the long-range strengthening mechanism of graphene monolayer in metal-graphene heterostructure as a super-strong nanomaterial and shock-wave transmitter during laser shock processing under room temperature(LSP) and cryogenic temperature (cLSP), respectively. Computational simulations, including finite element analysis and molecular dynamics simulation, were performed to investigate the shock wave propagation and dislocation evolution in graphene copper laminates.

2. Experiment methods

Three-layer graphene-copper laminated composite materials were used, with each copper layer a thickness of 30um and an average grain size around 100um. Samples were deformed by three processes with different strain rates and temperatures: 1) quasi-static compression. The load was 10 KN with a low strain rate of 0.05 s^{-1} using an MTS compression test machine. 2) room temperature laser shock peening The laser source was an Nd: YAG laser with a 1064 nm wavelength and 5 ns pulse width. The laser spot diameter was 2 mm and overlapping ratio was 50%. It was processed at room temperature with a power intensity of 6.5 GW cm^{-2} 3) cryogenic laser shock peening (cLSP). The sample was emerged in liquid nitrogen for 10 min until temperature stabilization, followed by cLSP processing with the same process parameters inLSP.

After deformation, hardness at different depths was measured by nanoindentation test using Agilent Technologies Nanoindenter G200 with a standard Berkovich diamond indenter with a load of 200 mN. To obtain the yield strength and study the deformation behavior, uniaxial micropillar compression tests were performed. Micropillars were fabricated by the focused ion beam (FIB) technique, and they have cylindrical geometry with the same diameter of ~3um and length of ~8um. The compression tests were performed using the Agilent Technologies Nanoindenter G200 with a diamond flat tip at room temperature. All experiments were conducted under a constant strain rate of 0.05 s^{-1} and the same displacement of 2000 nm with 1s hold. To characterize nanostructures after plastic deformation, transmission electron microscopy (TEM) experiments were performed using an FEI Talos 200X TEM operated at 200 kV . TEM images were made from copper at the second layer top surface for compressed, LSP and cLSP samples. To prepare the TEM samples, focused ion beam (FIB) technique was used by the FEI Nova 200 Dual Beam SEM/FIB: a) deposition of Pt on the sample surface as protection layer. b) ion-milling trenches around the sample. c) attaching the sample to the lift-out probe. d) lifting out the sample. e) attaching the sample to the TEM grid. f) thinning of the sample.

3. Results and discussions

3.1. Nanoindentation study of the heterostructure

Nanoindentation was an effective method to measure material strength, especially for nanomaterials and nanostructured materials. Zhang et al. measured the elastic modulus and indentation hardness of

nickel based superalloy [26]. Yang et al. [27] had studied the creep behaviors of copper with nanotwins and nanograins using indentation, and Liu et al. [28] investigated in situ indentation of nanoporous copper thin films with a pyramidal flat tip. To examine the work hardening effect on graphene-copper laminates by different processes, nano-indentation tests had been conducted. For each sample, hardness tests were performed at six different positions indicated by arrows in Fig. 2 b) inset. Load and displacement curves were obtained, and the curves at the first layer top surface were plotted in Fig. 2 a).

The hardness for the unprocessed sample was 0.95 GPa. Hardness distribution for samples after compression, LSP, and cLSP was shown in Fig. 2 b). All processed samples followed a similar trend, which has a peak hardness at the first layer and gradually decreased as depth increased. At the top surface (Position 1), hardness was greatly increased to 1.62 GPa, 1.67 GPa, and 1.8 GPa respectfully. After passing through one graphene layer (Position 3), an abrupt hardness decrease was observed for the compressed sample. For LSP/cLSP processed samples, however, no sharp decrements were found. As hardness decreased along with the depth, hardness at the bottom surface (Position 6) were 0.95 GPa, 1.07 GPa, and 1.11 GPa, respectively. Compared to the unprocessed sample, there was no hardness improvement for the compressed sample, but there were 12.6% and 16.8% increments after LSP/cLSP, respectively.

According to the hardness distribution, different work hardening effects were observed for compression and the LSP/cLSP process. Work hardening was limited to the first copper layer for compressed samples, but LSP/cLSP process could introduce work hardening further passing through the graphene layer. At the first copper layer (Position 1 and 2), hardness was increased, and work hardening was successfully achieved by all three different processes. When came to second and third copper layer, the compressed sample has neglectable hardness improvement and little work hardening could be observed, while LSP/cLSP samples have work hardening in the deeper layers.

3.2. Mechanical behaviors of the heterostructure during compression

Since a significant difference in hardness was found at the second layer top surface, micropillars were made at this position and compression tests were performed on these pillars to study the strength and deformation modes. As the size of the micropillars were orders of magnitude smaller than that of the grain, they were single crystal instead of polycrystalline. During compression of single crystal micropillar, plastic deformation was initiated as the applied stress was above the critical resolved shear stress. Plastic deformation might go through the glide stage and hardening stage. In the earlier glide stage, dislocations began to move on a specific slip system that has a maximum Schmidt factor. Shear stress was almost constant due to very few dislocation interactions. In the hardening stage, slip-on multiple slip systems were activated, and strong dislocation interactions occurred on intersecting slip planes. Shear stress would increase since dislocation tangles formed strong obstacles to dislocation motion.

Stress-strain curves for compressed, LSP, and cLSP samples were presented in Fig. 3 a). The compressed sample remained in the gliding stage during the test and exhibited yield stress of 125 MPa. LSP sample experienced a very short glide stage and went into the hardening stage, which showed enhanced yield strength of 175 MPa. As for the cLSP sample, easy glide started at 3% strain and hardening did not occur until 6% strain. The yield strength of the cLSP sample reached 220 MPa. The cLSP sample has the highest strength, which matches with the nano-indentation tests.

Fig. 3b)–d) showed Scanning Electron Microscopy (SEM) images of micropillars after compression tests, and different failure modes were found. For compressed sample (Fig. 3 b), only one single slip plane was observed. There was a large displacement in this slip orientation, indicating intense shear localization. Similar failure mode could be found on micropillar compression of single-crystal Ni [29] and AlTi intermetallic
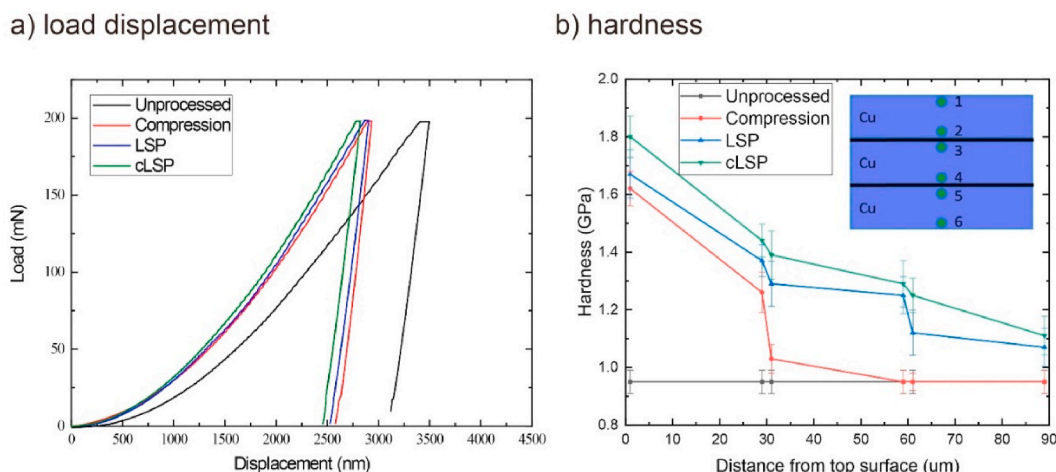
a) load displacement

b) hardness

Fig. 2. a) Loading-displacement relationship during nanoindentation tests of various processing conditions; b) hardness distribution with respect to depth of various processing conditions.
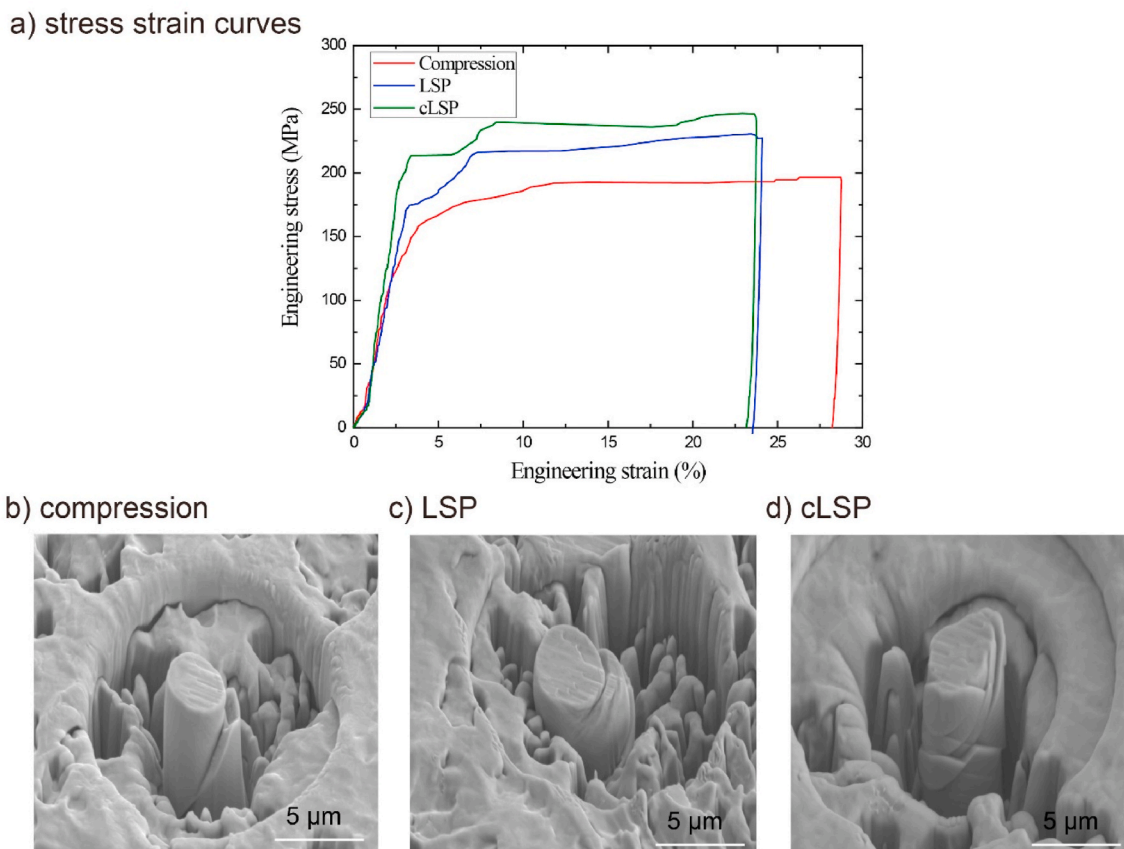
a) stress strain curves

b) compression

c) LSP

d) cLSP

Fig. 3. a) stress strain curves for micropillar compression test during nanoindentation tests of various processing conditions; b)-d) micropillars after compression tests for compression, LSP and cLSP processed samples.

[30]. Multiple slip bands with the same orientation were observed in the LSP sample, as shown in Fig. 3 c). When different slip planes were activated during the deformation, it corresponded to the hardening stage in the stress-strain curve. For the cLSP sample (Fig. 3 d), cross slip patterns were found which indicated a new slip system was also activated. Thus, glide and hardening were alternating during compression. Micropillars pre-deformed with high starting dislocation density also showed the same characteristics [31]. Different failure modes might be contributed by the different nanostructures generated by multiple

processes, which required further investigation.

3.3. Microstructure changes of the heterostructure after various processes

Three TEM samples were made from copper at the second layer top surface for compressed, LSP and cLSP samples, and dislocation substructures were presented in the Bright-field TEM images in Fig. 4a)–c). Those insets showed diffraction patterns at the [110] zone axis. The patterns have characteristic of single crystal since the size of TEM
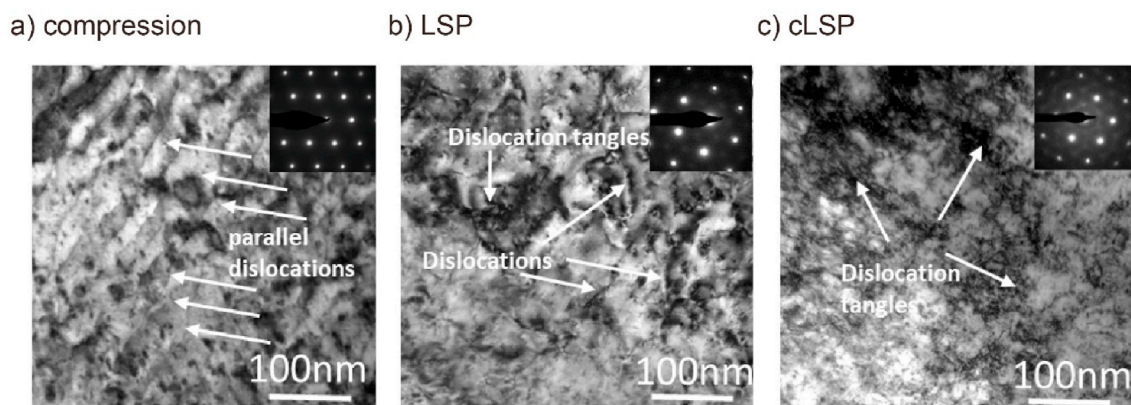
Fig. 4. a) TEM image for compression sample. b) TEM image for LSP sample. c) TEM image for cLSP sample.

samples were much smaller than that of coarse grain.

For the compressed sample, a small number of parallel dislocation arrays could be observed, indicated by the white arrows in Fig. 4 a). Similar patterns could be found on other deformed FCC metals such as aluminum after compression [32] and austenite after nanoindentation [33]. In the initial stage of compression, dislocations would be generated in the first copper layer and then blocked by the graphene interface. As compression continued, large barrier stress was surpassed to initiate dislocation emission at the neighboring layer. In the second copper layer top surface, only low-density dislocations could be generated. The small number of parallel dislocations introduced by the compression process was not able to block dislocation movements and activate more slip planes during the micropillar compression test, leading to a single slip and limited improvement in strength.

Fig. 4 b) showed dislocation lines and high-density dislocation

tangles on the copper layer below the graphene interface from the LSP sample. In the initial stage of the laser shock peening process, the first copper layer would be plastically deformed when the shock pressure was above copper dynamic yield stress. As shock waves propagated through the graphene interface, new dislocations would form easily at the following copper layer. Compared to the compressed sample, the LSP sample has a much higher dislocation density. These dislocation tangles could block dislocation movements and initiated new slip planes during the compression test, thus improving the hardness and strength. For the cLSP sample (Fig. 4 c), it was consisted of more uniformly distributed dislocation tangles. Similar phenomena happened on pure Al subjected to plastic deformation at liquid nitrogen temperature [34]. With more uniform and higher density pre-deformed dislocations, other slip systems could be triggered, and cross slip would happen. More details of the dislocation densities and distributions were elaborated with
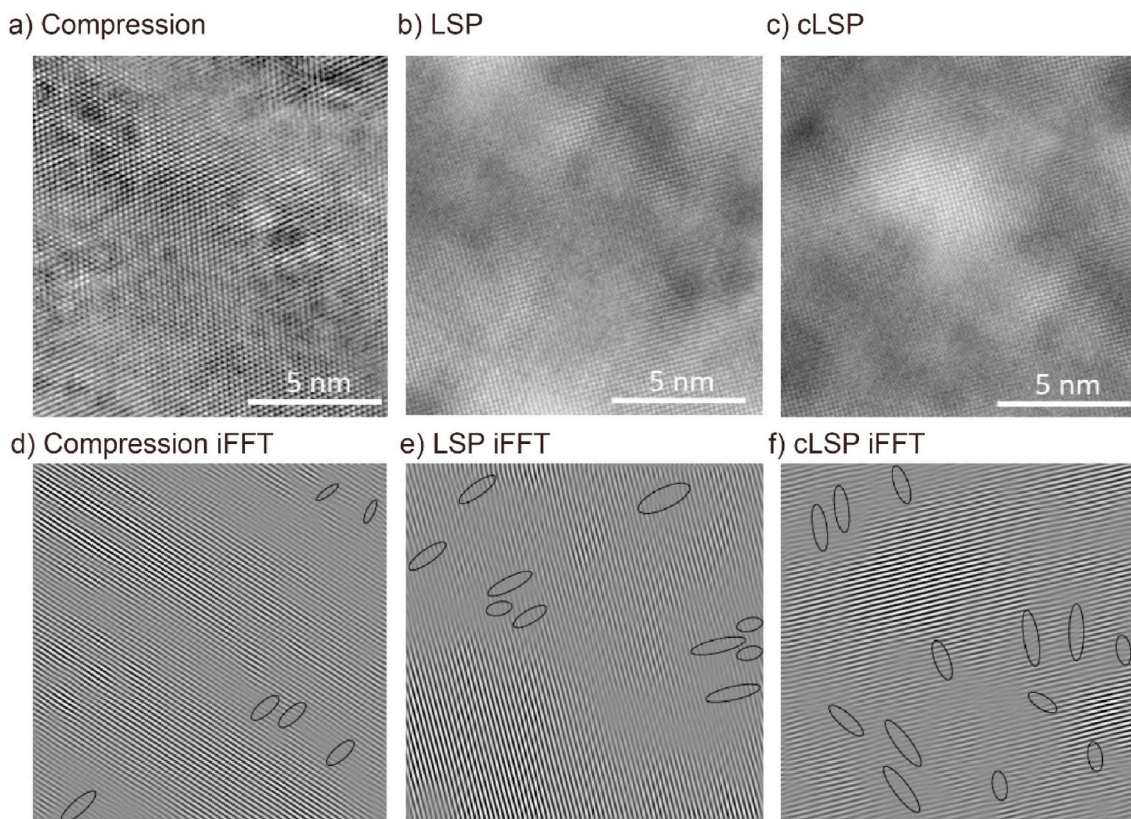

Fig. 5. a) HRTEM image for compression sample. b) HRTEM image LSP sample. c) HRTEM image for cLSP sample. d)-f) inverse Fast Fourier Transformation (IFFT) of HRTEM images for compression, LSP and cLSP processed samples.

high-resolution TEM images and its inverse Fourier Fast Transformation analysis presented in Fig. 5 a)-f). Dislocations were marked on these figures using black circles. As it could be seen, cLSP has the highest density dislocations and they were distributed uniformly, which contributes to higher strength while not reducing the ductility compared withLSP. Compression was low strain rate plastic deformation, LSP was room temperature high strain rate plastic deformation, and cLSP was lower temperature high strain rate plastic deformation. Both the stain rate and processing temperature could affect the dislocation generation process.

3.4. Understanding shock wave propagation in the heterostructure by FEM modeling

For a better understanding of the shock wave propagation and its interaction with graphene, Finite element modeling of the LSP of graphene-copper laminates (Fig. 6) was performed using the Abaqus commercial software. The 3D model was shown in Fig. 6 c). It consisted of three-layer copper with graphene as the interface. As a comparison, LSP of pure copper was also simulated with model presented in Fig. 6 b). Due to the symmetry of the specimen and the loading, only one-quarter symmetric cube was modeled. Uniform pressure was applied to the top surface as the load. For boundary conditions, symmetric displacement conditions were used for two laterals and fixed conditions were used for the bottom surface. The model was meshed by eight-node linear elements with reduced integration and hourglass control (C3D8R) and finer mesh was used close to the graphene interface. To avoid shock reflection at the substrate, infinite elements were used.

Constitutive model. The model contained two different materials, copper, and graphene. The interface between copper and graphene was modeled as surface-to-surface contact with tangential behavior of 0.3 friction coefficient. The graphene layer was modeled as elastic isotropic solids with an ultrahigh modulus of 1 TPa and Poisson ratio of 0.18. Since LSP was high strain rate process (LSP around 10^7 s^{-1}), the strain rate dependence of flow stress had to be taken into account. Austin et al. had developed a parameterized rate-dependent mechanisitic model for polycrystalline Cu [35]. Here, Johnson-Cook strain-rate sensitive plasticity model was used for the copper layer. The flow stress was given by:

$$\sigma = \left(\sigma_y + K\varepsilon_p^n\right)\left[1 + C\ln\left(\frac{\dot{\varepsilon}}{\dot{\varepsilon}_0}\right)\right]\left[1 - \left(\frac{T - T_0}{T_m - T_0}\right)^m\right] \qquad (1)$$

Where ε_p was the equivalent plastic strain, $\dot{\varepsilon}$ was the strain rate, and T was processing temperature (300K for LSP). σ_y, K, C, n, m, T_0, T_m were

material constants (For copper here, yield stress σ_y = 90 MPa, work hardening modulus K = 292 MPa, strain rate sensitivity C = 0.025, work hardening coefficient n = 0.31, m = 1.09, reference temperature T_0 = *294K*, melt temperature T_m = *1356K*).

Loading model. The shock pressure was given by [36]:

$$P(t) = P_{max} \cdot \overline{P}(t) \qquad (2)$$

Where P_{max} was the peak of shock wave pressure and $\overline{P}(t)$ was the normalized shock wave pressure distribution. According to the semi-empirical Fabro's model, the analytical form of P_{max} was:

$$P_{max} = 0.01\sqrt{\frac{\alpha}{2\alpha + 3}} \cdot \sqrt{\frac{2Z_1 Z_2}{Z_1 + Z_2}} \cdot \sqrt{I_P} \qquad (3)$$

Here I_P was the laser power intensity 6.5 GW cm^{-2} α was the laser-matter interaction efficiency ~0.1. Z_1 and Z_2 were the shock impedance of the confining layer (BK7 glass 4.18 *10^6 g cm^{-2} s^{-1}) and target (copper 1.44 *10^6 g cm^{-2} s^{-1}). Given that condition, the peak pressure was 6.6 GPa.

The temporal profile of the normalized shock pressure used was:

$$\overline{P}(t) = \begin{cases} \dfrac{(2k\tau - t)t}{(k\tau)^2} & 0 \leq t \leq k\tau \\[2mm] \exp\left(\ln 0.5\sqrt{\dfrac{t/\tau - k}{\eta - k/\sqrt{2}}}\right) & k\tau \leq t \leq m\tau \end{cases} \qquad (4)$$

Where τ was the laser pulse duration (5ns), $k\tau$ was the rising stage time (k = 1.5), η was the ratio of pressure width and pulse width (η = 2.5). The shock pressure used in this study was shown in Fig. 6 a).

To look more closely for shock wave propagation without and with graphene layer, stress contours were shown in Fig. 7. Fig. 7 a) and 7 d) presented the stress distribution in pure copper and graphene copper laminates in the early stage, the deep blue region was the shock pressure peak and no significant difference was observed yet. In Fig. 7 b), the deep blue region was moving down which meant the shock wave was propagating in the copper. Great difference could be observed for graphene copper laminates, as shown in Fig. 7 e). The deep blue region had passed the graphene layer, and a light blue region was shown above the graphene layer which represented the bounced shock wave. Similar stress distribution could be seen as shock wave propagated through the second graphene layer, as shown in Fig. 7 f). Simulation results had clearly showed that part of the shock wave was reflected as it interacted with graphene layer. Also, shock wave pressure was gradually
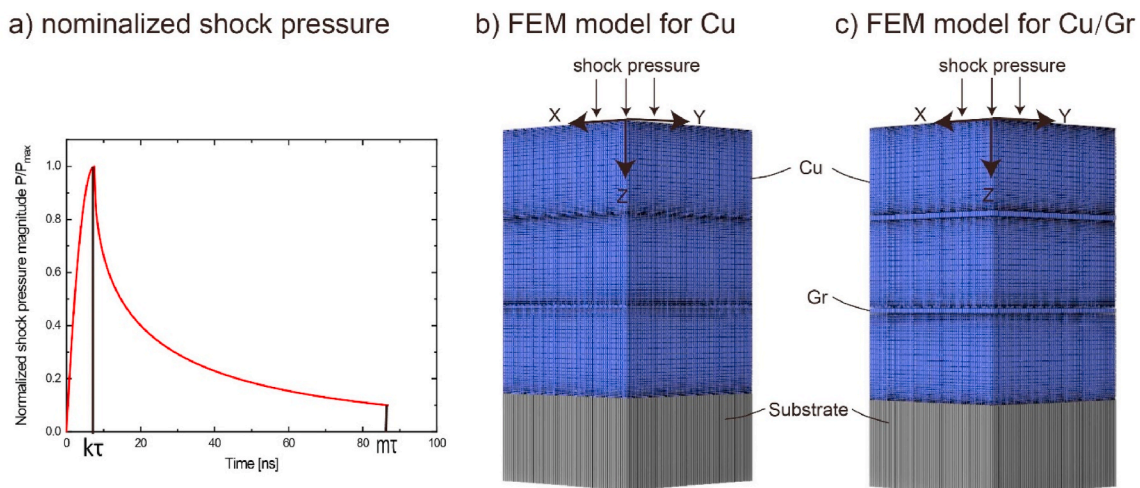

Fig. 6. a) normalized shock pressure temporal profile induced by 5ns laser pulse. b) Finite element discretization for copper. c) Finite element discretization for copper graphene composite.
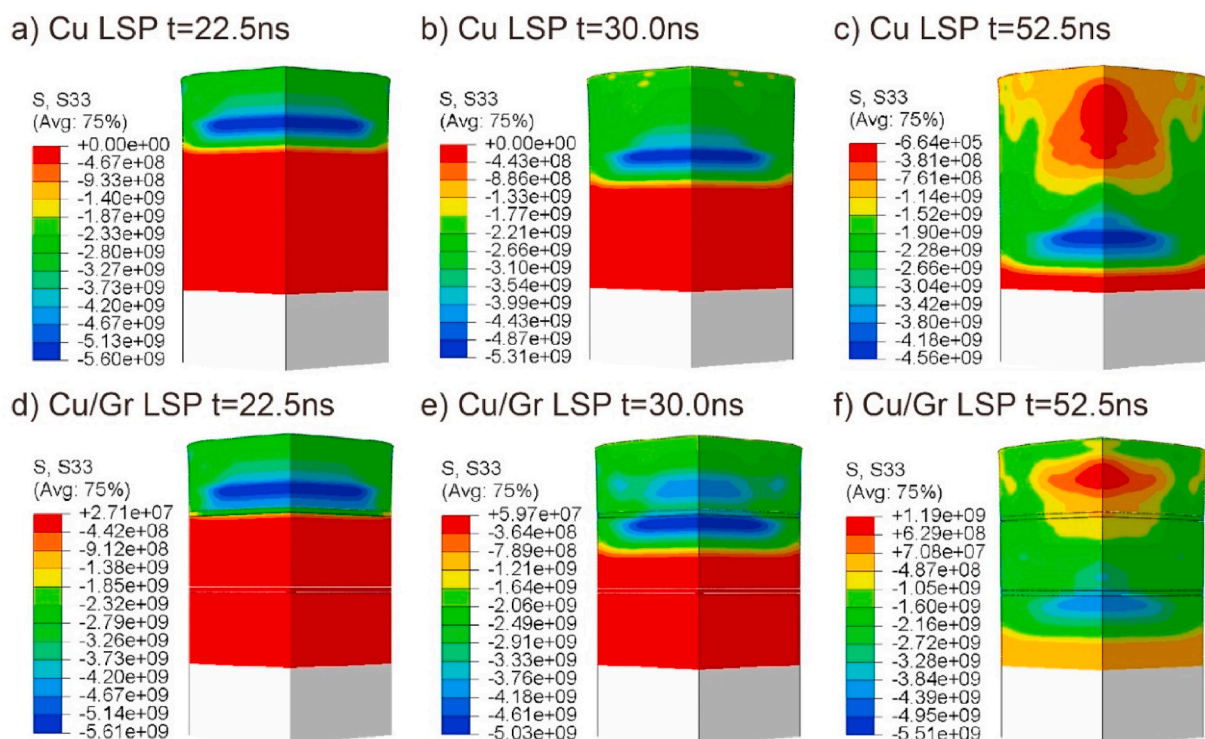
Fig. 7. a)-c) stress distribution for LSP processed copper at t = 22.5ns, 30.0ns and 52.5ns. d)-f) stress distribution for LSP processed copper graphene at t = 22.5ns, 30.0ns and 52.5ns.

attenuated as it propagated into the sample, which accounted for the gradual decrease in hardness.

Fig. 8 a) and c) presented stresses evolution along the z centerline at 7.5ns, 15ns, 22.5ns, 30ns, 37.5ns, 45ns, 52.5ns for pure copper and graphene copper laminates. At t = 7.5ns, stress at the top surface (depth = 0 um) reached its peak value 6.6 GPa. As it propagated through the copper layer, the magnitude of peak stress gradually reduced to 6.1 GPa (depth = 20um). At t = 30ns, the peak shock wave passed through the graphene layer. The stress distribution of graphene copper laminates were different from the one of pure copper as marked by the dashed ellipse. Larger compressive stress was presented near graphene layer of copper graphene laminates, which was corresponding to the light blue region in Fig. 7 e). This demonstrated that part of the shock wave was bounced back when the shock wave interacted with the graphene interface. A similar phenomenon could be observed when the shock wave passed the next graphene layer at t = 52.5ns. The result showed that shock waves could pass through the graphene layers and part of it could be bounced back by the graphene interface. Simulation results had been validated by the hardness distribution for pure copper and graphene copper laminates in Fig. 8 b) and d). For pure copper after LSP, the hardness gradually reduced since the shock wave was attenuated (as shown in Fig. 8 a). Fig. 8 d) had shown the local hardness improvement contributed by graphene. At Position 2, the lowest hardness was 1.15 GPa and it was increased to 1.32 GPa (14.7%); Position 4, the lowest hardness was 0.99 GPa and it was increase to 1.11 GPa (12%). As we can see, the hardness was locally increasing instead of decreasing due to shock wave attenuation as it approached graphene layer of graphene copper laminates (Fig. 8d). The high hardness near graphene layer indicated the shock wave reflection at graphene interface.

Based on the above FEM simulation results, we could see that the shock propagation and hardness could be greatly changed by adding only a few amounts of graphene (1.42×10^{-6}% vol.). For pure copper, the shock wave could propagate forward freely leading to a gradually reduced hardness distribution. By adding several layers of graphene with thirty micros in distance, shock wave would be partially reflected at

the copper graphene interface due to their different material properties (such as density and wave velocity). This interactions between shock wave and graphene yielded the local increase in stress and hardness. As a result, the reflection wave introduced by graphene layer had a large influence on material properties.

3.5. Understanding the microstructure changes by MD simulation

Our experiment had shown significant differences in dislocation structures after the graphene layer under different loads. It would be interesting to investigate the dislocation generation and evolution process. Here we used the Large-scale Atomic/Molecular Massively Parallel Simulator (LAMMPS) for non-equilibrium MD simulations of shock loading copper/graphene heterostructure.

As shown in Fig. 9 a), a small portion at the copper graphene interface was studied at the atomistic scale. The initial configuration had 128,328 atoms (red marked atoms were copper and blue marked atoms were carbon) and the dimension of the simulation box was $10 \times 9 \times 17$ nm ^{3}. The embedded atom model potential (EAM) was used to compute pairwise interactions of Cu–Cu atoms. The interactions between C–C atoms were described by the adaptive intermolecular reactive empirical bond order potential (AIREBO). Cu–C interactions were described by the 12-6 Lennard-Jones type of van der Waal's interaction with well depth 0.025 eV and equilibrium distance 3.0825 Å. The system was equilibrated at 300 K (for LSP)/77 K (for cLSP) and zero pressure using the constant temperature and pressure ensemble (NPT) with a time step 1 fs. Shock loading was applied along the z-direction, normal to the graphene layer. For shock loading, a constant velocity of 1200 m/s was assigned to the simulation box bottom plane and impacted on the copper atoms [37, 38]. Periodic boundary conditions were used for x- and y-directions, and free surface conditions for the shock loading z-direction.

Fig. 9b) and c) presented dislocation evolution for LSP and cLSP processed graphene copper laminates after Dislocation Extraction Algorithm (DXA) analysis of MD simulation results using Ovito [39]. When laser shock was initially applied (t = 1.4ps), dislocations were generated
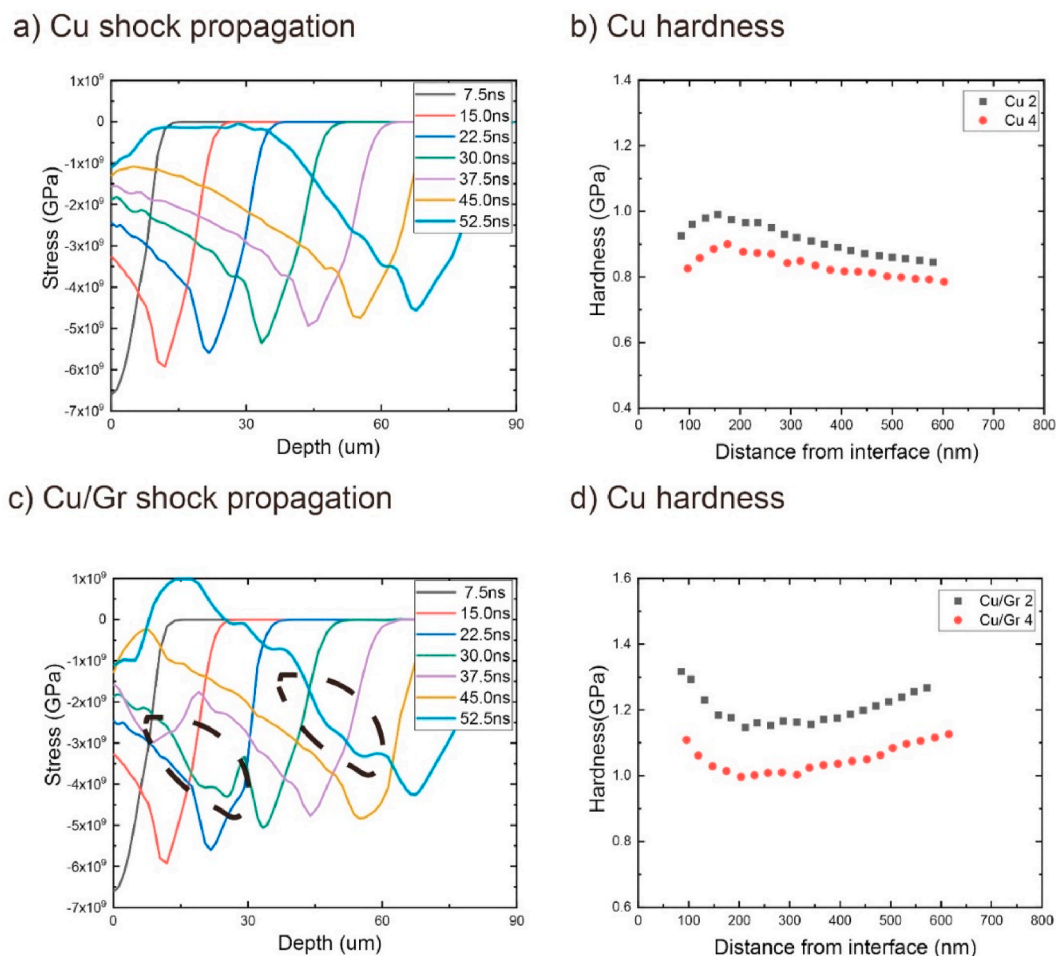
Fig. 8. a) shock wave propagation in *z* direction for LSP processed copper. b) experimental hardness distribution for LSP processed copper measured at location 2 and location 4. c) shock wave propagation in *z* direction for LSP processed copper graphene composite. d) hardness distribution for LSP processed copper graphene composite measured at location 2 and location 4.

at the bottom copper layer and blocked by the graphene interface. No dislocations were found at the neighboring copper layer. As the shock wave propagated through graphene along Z direction (t = 2.1ps, 2.8ps), new dislocations were formed at the neighboring layer. The total length of dislocation lines obtained from DXA analysis was summarized in Fig. 9d), and the temperature effect could be observed. Dislocation generation was lagged for cryogenic laser shock peening and lower dislocation density was found in the earlier stage. This was because the yield strength was higher at a lower temperature, thus making it harder to initiate plastic deformation. However, in the later stage, dislocations were generated more rapidly in cLSP, which wasdue to the reduced dislocation mobilities and less dislocation annihilation under lower processing temperature. As dynamic recovery was suppressed, more dislocations were accumulated. Besides that, wave propagated faster at cryogenic temperature, and it resulted in stronger interaction between shock wave and graphene interface. The calculated dislocation densities were 3.92×10^{17} m^{-2} (LSP) and 5.23×10^{17} m^{-2} (cLSP) respectively. MD simulations showed higher dislocation density at a lower temperature, which matched well with TEM results. The higher density dislocations and their uniform distributions contributed to the higher strength. The stress-strain curves during mechanical loading were presented in Fig. 9e). It was shown that cLSP leads to higher yield strength than LSP, while it had limited effects on the elastic modulus.

A close look at the atomic configuration evolution after LSP and cLSP was presented in Fig. 10. The green marked atoms were FCC structure, and red marked ones were HCP structure. As shown, the majority of the atoms remained FCC structure during the laser shock peeing process. Initially, dislocations were limited at the bottom side. As time evolved, some dislocations could be generated across the graphene surface. More and more dislocations could be formed as stress wave propagated. Defect analysis showed that dislocations were generated on different slip planes and distributed uniformly in the copper layer, which matched with the dislocation tangles found in the TEM images.

4. Conclusion

In summary, the mechanical behavior of layered graphene-copper heterostructures was studied as result of compression, laser shock peening, and cryogenic laser shock peening, in order to understand the graphene-metal composite's strengthening mechanism under extremely low graphene concentration. Nanoindentation and micropillar compression tests were performed to study the mechanical properties, and TEM samples were made to investigate the underlying nanostructures. Finite element modeling was adopted to study the wave propagation in the heterostructure, while atomistic scale MD simulation was utilized to study the dislocation evolution during the laser shock peening process under room and cryogenic temperatures. The yield stress was 125 MPa, 175 MPa, and 220 MPa for compressed, LSP, and cLSP samples, respectively. Hardness and yield stress were larger in LSP/cLSP sample as opposed to the compressed one, and it was more obvious on the second layer top surface. A significant difference in strength and deformation mode among them was originated from different
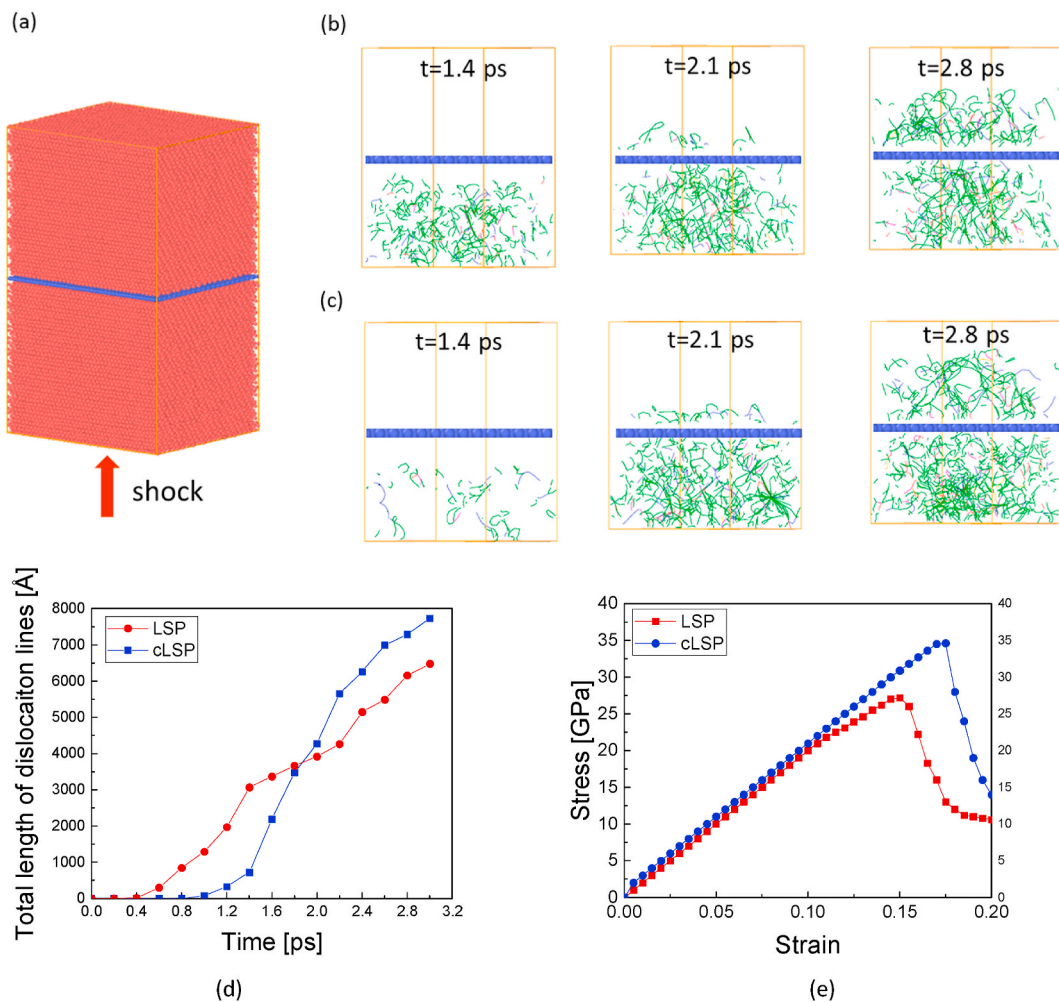
Fig. 9. MD simulation. a) atomic configuration of graphene copper composite; b)&c) DXA analysis for LSP and cLSP at different time steps 1.4ps, 2.1ps and 2.8ps. d) dislocation length along time; e) stress strain curve.
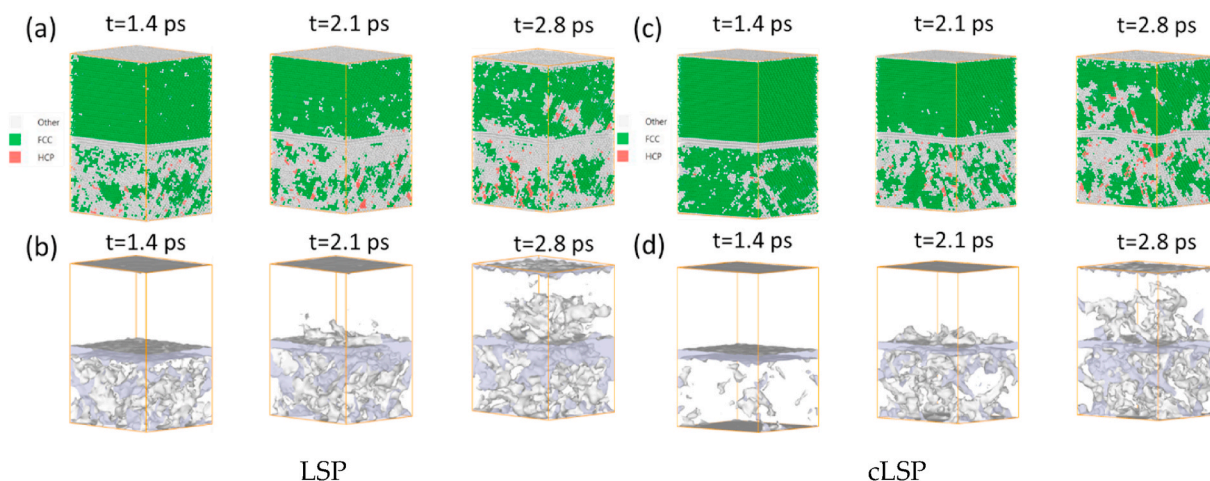

LSP   cLSP

Fig. 10. MD simulation results for LSP (a, b) and cLSP (c, d) at different time steps 1.4ps, 2.1ps and 2.8ps. a)&c) atomic structure distribution (the green represents fcc structure and the red represent hcp structure) for LSP and cLSP respectively; b)&d) defects for LSP and cLSP respectively. (For interpretation of the references to colour in this figure legend, the reader is referred to the Web version of this article.)

dislocation densities and distributions. The small number of parallel dislocation arrays was found by compression around the graphene interface, while high density dislocation tangles could be generated beyond the graphene interface by LSP/cLSP, resulting in higher

strength. In addition, it is found that decreasing processing temperature in LSP leads to higher dislocation density and higher strength. This higher density was observed during cLSP than LSP due to the refrained dislocation recovery activity at a lower temperature, resulting in a 28%

increment in strength when the temperature went down from room temperature to liquid nitrogen temperature. Compared with static compression, the laser shock wave can pass through the graphene layer and introduce dislocations beneath it, thus strengthening the material. Unlike the fully transmitted case in pure copper, graphene layers interact with the shock wave, and part of the shock wave is reflected. Decreasing processing temperature, faster wave propagation also contributes to higher dislocation density and strength. This work indicated that LSP/cLSP laser shock peening process could be utilized to improve the mechanical properties by introducing high density dislocations for graphene-based metal composite.

CRediT authorship contribution statement

Sen Xiang: carried out experiments, simulation and analyzed the data, wrote the paper. **Xingtao Liu:** performed the microstructure characterization. **Rong Xu:** helped in the micro-compression testing. **Kejie Zhao:** helped in the micro-compression testing. **Dong Lin:** conducted experiments and testing using nanoindentation at earlier stage of the work. **Fei Yin:** conducted experiments and microstructure characterization. **Gary J. Cheng:** conceptualized this study, wrote the paper.

Declaration of competing interest

The authors declare that they have no known competing financial interests or personal relationships that could have appeared to influence the work reported in this paper.

Acknowledgements

Appendix A. Supplementary data

Supplementary data to this article can be found online at https://doi.org/10.1016/j.msea.2022.142741.

References

[1] G. Song, Z. Wang, Y. Gong, Y. Yang, Q. Fu, C. Pan, Direct determination of graphene amount in electrochemical deposited Cu-based composite foil and its enhanced mechanical property, RSC Adv. 7 (3) (2017) 1735–1742.

[2] G. Huang, et al., Preparation and characterization of the graphene-Cu composite film by electrodeposition process, Microelectron. Eng. 157 (2016) 7–12.

[3] D. Lin, C. Richard Liu, G.J. Cheng, Single-layer graphene oxide reinforced metal matrix composites by laser sintering: microstructure and mechanical property enhancement, Acta Mater. 80 (2014) 183–193.

[4] K. Chu, C. Jia, Enhanced strength in bulk graphene-copper composites, Phys. Status Solidi Appl. Mater. Sci. 211 (1) (2014) 184–190.

[5] D. Lin, et al., Shock engineering the additive manufactured graphene-metal nanocomposite with high density nanotwins and dislocations for ultra-stable mechanical properties, Acta Mater. 150 (2018) 360–372.

[6] C. Ye, Y. Liao, S. Suslov, D. Lin, G.J. Cheng, Ultrahigh dense and gradient nano-precipitates generated by warm laser shock peening for combination of high strength and ductility, Mater. Sci. Eng., A 609 (2014) 195–203.

[7] Y. Kim, et al., Strengthening effect of single-atomic-layer graphene in metal-graphene nanolayered composites, Nat. Commun. 4 (2013).

[8] L. Zhao, et al., Strain-rate dependent deformation mechanism of graphene-Al nanolaminated composites studied using micro-pillar compression, Int. J. Plast. 105 (February) (2018) 128–140.

[9] P.K. Prashantha, et al., Enhanced surface and mechanical properties of bioinspired nanolaminate graphene-aluminum alloy nanocomposites through laser shock processing for engineering applications, Mater. Today Commun. 16 (April) (2018) 81–89.

[10] A. Misra, J.P. Hirth, R.G. Hoagland, Length-scale-dependent deformation mechanisms in incoherent metallic multilayered composites, Acta Mater. 53 (18) (2005) 4817–4824.

[11] A.V. Podolskiy, H.P. Ng, I.A. Psaruk, E.D. Tabachnikova, R. Lapovok, Cryogenic equal channel angular pressing of commercially pure titanium: microstructure and properties, J. Mater. Sci. 49 (19) (2014) 6803–6812.

[12] D.C.C. Magalhães, A.M. Kliauga, M. Ferrante, V.L. Sordi, Plastic deformation of FCC alloys at cryogenic temperature: the effect of stacking-fault energy on microstructure and tensile behaviour, J. Mater. Sci. 52 (12) (2017) 7466–7478.

[13] W. Zhou, X. Ren, Y. Yang, Z. Tong, E. Asuako Larson, Finite element analysis of laser shock peening induced near-surface deformation in engineering metals, Opt Laser. Technol. 119 (October 2018) 2019.

[14] S.M.E. North, S. Sunny, G. Gleason, ScienceDirect predictive modeling of laser shock peening induced near-surface residual predictive predictive modeling modeling of of laser laser shock shock peening peening induced induced near-surface near-surface residual residual stress in alumina Stre, Procedia Manuf. 53 (2021) 80–91.

[15] Z. He, et al., Surface & Coatings Technology Laser shock peening regulating aluminum alloy surface residual stresses for enhancing the mechanical properties : roles of shock number and energy, Surf. Coating. Technol. 421 (July) (2021) 127481.

[16] N. Hfaiedh, P. Peyre, H. Song, I. Popa, V. Ji, V. Vignal, Finite element analysis of laser shock peening of 2050-T8 aluminum alloy, Int. J. Fatig. 70 (2015) 480–489.

[17] Y. Yang, W. Zhou, Z. Tong, L. Chen, X. Ren, Delamination in titanium-based carbon-fibre/epoxy laminates under laser shock peening, Opt Laser. Technol. 143 (December 2020) (2021) 107282.

[18] J. Kim, K. Kang, S. Ryu, Characterization of the misfit dislocations at the ferrite/cementite interface in pearlitic steel: an atomistic simulation study, Int. J. Plast. 83 (2016) 302–312.

[19] M. Damadam, S. Shao, I. Salehinia, I. Mastorakos, G. Ayoub, H.M. Zbib, Strength and plastic deformation behavior of nanolaminate composites with pre-existing dislocations, Comput. Mater. Sci. 138 (2017) 42–48.

[20] I. Salehinia, J. Wang, D.F. Bahr, H.M. Zbib, Molecular dynamics simulations of plastic deformation in Nb/NbC multilayers, Int. J. Plast. 59 (2014) 119–132.

[21] J.Q. Zhu, Q.S. Yang, X. Liu, Investigation on the tensile behavior of graphene-aluminum nano-laminated composites by molecular dynamics simulation, Key Eng. Mater. 804 (2019) 1–6. KEM.

[22] H. Ning, et al., Molecular dynamics study of strengthening mechanism of nanolaminated graphene/Cu composites under compression, Sci. Rep. 8 (1) (2018) 1–10.

[23] X. Liu, J. Cai, S.N. Luo, Interfacial anti-fatigue effect in graphene-copper nanolayered composites under cyclic shear loading, Phys. Chem. Chem. Phys. 20 (11) (2018) 7875–7884.

[24] K. Wang, S. Xiao, H. Deng, W. Zhu, W. Hu, An atomic study on the shock-induced plasticity and phase transition for iron-based single crystals, Int. J. Plast. 59 (2014) 180–198.

[25] P.S. Branicio, A. Nakano, R.K. Kalia, P. Vashishta, Shock loading on AlN ceramics: a large scale molecular dynamics study, Int. J. Plast. 51 (2013) 122–131.

[26] Y. Zhang, D.P. Mohanty, P. Seiler, T. Siegmund, J.J. Kruzic, V. Tomar, High temperature indentation based property measurements of IN-617, Int. J. Plast. 96 (2017) 264–281.

[27] X.S. Yang, et al., Time-, stress-, and temperature-dependent deformation in nanostructured copper: creep tests and simulations, J. Mech. Phys. Solid. 94 (2016) 191–206.

[28] R. Liu, S. Pathak, W.M. Mook, J.K. Baldwin, N. Mara, A. Antoniou, In situ frustum indentation of nanoporous copper thin films, Int. J. Plast. 98 (2017) 139–155.

[29] D.M. Dimiduk, M.D. Uchic, T.A. Parthasarathy, Size-affected single-slip behavior of pure nickel microcrystals, Acta Mater. 53 (15) (2005) 4065–4077.

[30] K. Edalati, Z.J. Horita, High strength and high ductility in nanostructured aluminium-based intermetallics produced by high-pressure torsion, Mater. Sci. Forum 765 (2013) 558–562.

[31] J.A. El-Awady, et al., Pre-straining effects on the power-law scaling of size-dependent strengthening in Ni single crystals, Scripta Mater. 68 (3–4) (2013) 207–210.

[32] L. Zhao, et al., Strain-rate dependent deformation mechanism of graphene-Al nanolaminated composites studied using micro-pillar compression, Int. J. Plast. 105 (Jun. 2018) 128–140.

[33] T. Chen, L. Tan, Z. Lu, H. Xu, The effect of grain orientation on nanoindentation behavior of model austenitic alloy Fe-20Cr-25Ni, Acta Mater. 138 (Oct. 2017) 83–91.

[34] F. Huang, N.R. Tao, Effects of strain rate and deformation temperature on microstructures and hardness in plastically deformed pure aluminum, J. Mater. Sci. Technol. 27 (1) (2011) 1–7.

[35] R.A. Austin, D.L. McDowell, Parameterization of a rate-dependent model of shock-induced plasticity for copper, nickel, and aluminum, Int. J. Plast. 32 (33) (2012) 134–154.

[36] C. Wang, X. Wang, Y. Xu, Z. Gao, Numerical modeling of the confined laser shock peening of the OFHC copper, Int. J. Mech. Sci. 108–109 (2016) 104–114.

[37] E.N. Hahn, T.C. Germann, R. Ravelo, J.E. Hammerberg, M.A. Meyers, On the ultimate tensile strength of tantalum, Acta Mater. 126 (2017) 313–328.

[38] D. Seif, G. Po, R. Crum, V. Gupta, N.M. Ghoniem, Shock-induced plasticity and the Hugoniot elastic limit in copper nano films and rods, J. Appl. Phys. 115 (5) (2014).

[39] A. Stukowski, V.V. Bulatov, A. Arsenlis, Automated identification and indexing of dislocations in crystal interfaces, Model. Simulat. Mater. Sci. Eng. 20 (8) (2012).